Supplementary Information to: Unified adiabatic and diabatic excited-state description *via* the ensemble-variational quantum eigensolver

Christophe Soule,[a] Bruno Senjean[a] and Benjamin Lasorne[a]*

May 19, 2026

1 Concepts and Methods

1.1 Various flavors of the eigenproblem objective

To analyze the stability of the functions f^{F} defined Eq. 24 and f^{W} defined Eq. 29, we consider small variations $\{\delta H'_{II}\}_{I\in\{A,B,C\}}$ in the diagonal components $\{H'_{II}\}_{I\in\{A,B,C\}}$, resulting from perturbations of the rotation angles (θ,ϕ,ψ). We define $\delta f = f(H+\delta H) - f(H)$, leading to

$$\delta f^{\mathrm{F}} = -\sum_{I\in\{A,B,C\}} \left(2H'_{II}\,\delta H'_{II} + (\delta H'_{II})^2\right) \quad , \tag{S1a}$$

$$\delta f^{\mathrm{W}} = \sum_{I\in\{A,B,C\}} w_I\,\delta H'_{II} \quad . \tag{S1b}$$

While f^{W} varies directly with perturbations in the energies, f^{F} varies proportionally to the energies themselves. This analysis can be related to classical sensitivity analysis, which aims at estimating the variation of an objective function induced by small perturbations of the underlying parameters[1]. A more detailed analysis of such aspects will be provided in future work.

2 Computational Details

2.1 Molecular-orbital representation

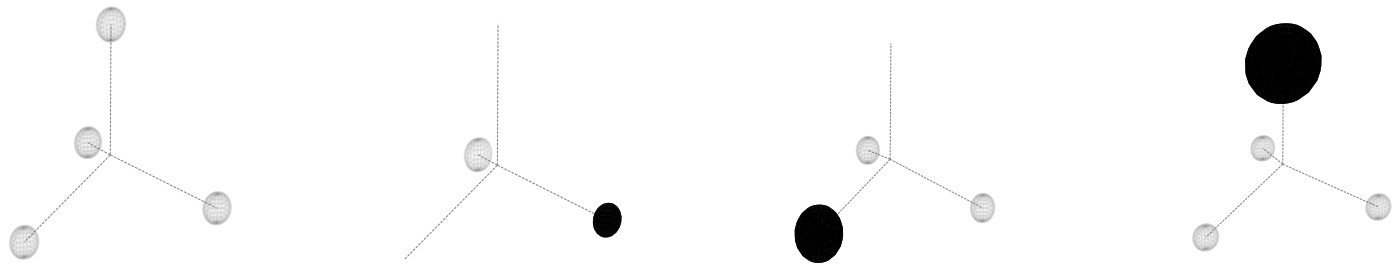

(a) a_1 orbital **(b)** t_2 orbital **(c)** t_2 orbital **(d)** t_2 orbital

Figure S1 Molecular-orbital representation of H_4^+ in the tetrahedral geometry

2.2 Implementation of the change of basis under a similarity transformation

In the following, we describe the sequence of quantum operations implemented in the circuits, shown in Table 2, for preparing the states $\left|\Phi_{\mathrm{A}}^{0\prime}(\theta,\phi,\psi)\right\rangle$, $\left|\Phi_{\mathrm{B}}^{0\prime}(\theta,\phi,\psi)\right\rangle$, and $\left|\Phi_{\mathrm{C}}^{0\prime}(\theta,\phi,\psi)\right\rangle$ of the $a_1^2t_2^1$-open-shell H_4^+ system from the initial state $|10001000\rangle$ corresponding to various ways of adding one extra α-electron (into the t_2-manifold) to the a_1^2-closed-shell H_4^{2+} system. The latter is first prepared by applying X gates to qubits 1 and 5. Here, $X_{(i)}$, $Z_{(i)}$, $R_{\boldsymbol{y}}(\theta)_{(i)}$ denote X, Z, $R_{\boldsymbol{y}}(\theta)$ quantum gates with target qubit i. Moreover, $CX_{(i,j)}$ and $CR_{\boldsymbol{y}}(\theta)_{(i,j)}$ denote controlled-X and controlled-$R_{\boldsymbol{y}}(\theta)$ quantum gates, respectively, with control qubit i and target qubit j.

2.2.1 Quantum circuit for preparing the state $\left|\Phi_{\mathrm{A}}^{0\prime}(\theta,\phi,\psi)\right\rangle$

$R_{\mathbf{y}}(2\psi)_{(3)}$

$$\cos(\psi)\,|10001000\rangle + \sin(\psi)\,|10101000\rangle \tag{S2}$$

$CX_{(3,2)}$

$$\cos(\psi)\,|10001000\rangle + \sin(\psi)\,|11101000\rangle \tag{S3}$$

[a]ICGM, Univ Montpellier, CNRS, ENSCM, Montpellier, France
*Corresponding author: benjamin.lasorne@umontpellier.fr

$X_{(2)}$

$$\cos(\psi)\,|11001000\rangle + \sin(\psi)\,|10101000\rangle \tag{S4}$$

$CR_{\mathbf{y}}(2\phi)_{(2,4)}$

$$\cos(\phi)\cos(\psi)\,|11001000\rangle + \sin(\phi)\cos(\psi)\,|11011000\rangle + \sin(\psi)\,|10101000\rangle \tag{S5}$$

$CX_{(4,2)}$

$$\cos(\phi)\cos(\psi)\,|11001000\rangle + \sin(\phi)\cos(\psi)\,|10011000\rangle + \sin(\psi)\,|10101000\rangle \tag{S6}$$

$CX_{(3,4)}$

$$\cos(\phi)\cos(\psi)\,|11001000\rangle + \sin(\phi)\cos(\psi)\,|10011000\rangle + \sin(\psi)\,|10111000\rangle \tag{S7}$$

$CX_{(4,3)}$

$$\cos(\phi)\cos(\psi)\,|11001000\rangle + \sin(\phi)\cos(\psi)\,|10111000\rangle + \sin(\psi)\,|10011000\rangle \tag{S8}$$

$CR_{\mathbf{y}}(2\theta)_{(4,3)}$

$$\begin{aligned}&\cos(\phi)\cos(\psi)\,|11001000\rangle - \sin(\theta)\sin(\phi)\cos(\psi)\,|10011000\rangle + \cos(\theta)\sin(\phi)\cos(\psi)\,|10111000\rangle\\&+\cos(\theta)\sin(\psi)\,|10011000\rangle + \sin(\theta)\sin(\psi)\,|10111000\rangle\end{aligned} \tag{S9}$$

$CX_{(3,4)}$

$$\begin{aligned}&\cos(\phi)\cos(\psi)\,|11001000\rangle - \sin(\theta)\sin(\phi)\cos(\psi)\,|10011000\rangle + \cos(\theta)\sin(\phi)\cos(\psi)\,|10101000\rangle\\&+\cos(\theta)\sin(\psi)\,|10011000\rangle + \sin(\theta)\sin(\psi)\,|10101000\rangle\end{aligned} \tag{S10}$$

$Z_{(4)}$

$$\begin{aligned}&\cos(\phi)\cos(\psi)\,|11001000\rangle + (\sin(\theta)\sin(\phi)\cos(\psi) - \cos(\theta)\sin(\psi))\,|10011000\rangle\\&+(\cos(\theta)\sin(\phi)\cos(\psi) + \sin(\theta)\sin(\psi))\,|10101000\rangle\end{aligned} \tag{S11}$$

2.2.2 Quantum circuit for preparing the state $\left|\Phi_{\mathrm{B}}^{0\prime}(\theta,\phi,\psi)\right\rangle$

$R_{\mathbf{y}}(2\phi)_{(2)}$

$$\cos(\phi)\,|10001000\rangle + \sin(\phi)\,|11001000\rangle \tag{S12}$$

$CX_{(2,3)}$

$$\cos(\phi)\,|10001000\rangle + \sin(\phi)\,|11101000\rangle \tag{S13}$$

$X_{(3)}$

$$\cos(\phi)\,|10101000\rangle + \sin(\phi)\,|11001000\rangle \tag{S14}$$

$R_{\mathbf{y}}(2\theta)_{(3,4)}$

$$\cos(\theta)\cos(\phi)\,|10101000\rangle + \sin(\theta)\cos(\phi)\,|10111000\rangle + \sin(\phi)\,|11001000\rangle \tag{S15}$$

$CX_{(4,3)}$

$$\cos(\theta)\cos(\phi)\,|10101000\rangle + \sin(\theta)\cos(\phi)\,|10011000\rangle + \sin(\phi)\,|11001000\rangle \tag{S16}$$

$Z_{(2)}$

$$\cos(\theta)\cos(\phi)\,|10101000\rangle + \sin(\theta)\cos(\phi)\,|10011000\rangle - \sin(\phi)\,|11001000\rangle \tag{S17}$$

2.2.3 Quantum circuit for preparing the state $\left|\Phi_{\mathrm{C}}^{0\prime}(\theta,\phi,\psi)\right\rangle$

$R_{\mathbf{y}}(2\psi)_{(2)}$

$$\cos(\psi)\,|10001000\rangle + \sin(\psi)\,|11001000\rangle \tag{S18}$$

$CX_{(2,4)}$

$$\cos(\psi)\,|10001000\rangle + \sin(\psi)\,|11011000\rangle \tag{S19}$$

$X_{(4)}$

$$\cos(\psi)\,|10011000\rangle + \sin(\psi)\,|11001000\rangle \tag{S20}$$

$CR_{\mathbf{y}}(2\phi)_{(2,3)}$

$$\cos(\psi)\,|10011000\rangle + \cos(\phi)\sin(\psi)\,|11001000\rangle + \sin(\phi)\sin(\psi)\,|11101000\rangle \tag{S21}$$

$CX_{(3,2)}$

$$\cos(\psi)\,|10011000\rangle + \cos(\phi)\sin(\psi)\,|11001000\rangle + \sin(\phi)\sin(\psi)\,|10101000\rangle \tag{S22}$$

$CX_{(4,3)}$

$$\cos(\psi)\,|10111000\rangle + \cos(\phi)\sin(\psi)\,|11001000\rangle + \sin(\phi)\sin(\psi)\,|10101000\rangle \tag{S23}$$

$CR_{\mathrm{y}}(2\theta)_{(3,4)}$

$$\begin{aligned} &-\sin(\theta)\cos(\psi)\,|10101000\rangle + \cos(\theta)\cos(\psi)\,|10111000\rangle + \cos(\phi)\sin(\psi)\,|11001000\rangle \\ &+\cos(\theta)\sin(\phi)\sin(\psi)\,|10101000\rangle + \sin(\theta)\sin(\phi)\sin(\psi)\,|10111000\rangle \end{aligned} \tag{S24}$$

$CX_{(4,3)}$

$$(\cos(\theta)\sin(\phi)\sin(\psi) - \sin(\theta)\cos(\psi))\,|10101000\rangle + (\cos(\theta)\cos(\psi) + \sin(\theta)\sin(\phi)\sin(\psi)\,|10011000\rangle + \cos(\phi)\sin(\psi)\,|11001000\rangle \tag{S25}$$

3 Results and Discussion

3.1 Distortion within C_1 geometry (from $\Delta x_2 = 0.1$ Å and $\Delta y_3 = 0.05$ Å): impact of the initial guess states

For illustration purposes, we deliberately tried an optimization from a "wrong guess" (doubly excited configurations): $|\Phi_{\mathrm{A}}^0\rangle = |11000001\rangle$, $|\Phi_{\mathrm{B}}^0\rangle = |10100001\rangle$, and $|\Phi_{\mathrm{C}}^0\rangle = |10010001\rangle$. In these, the β-electron now occupies the third excited orbital and the totally-bonding orbital is singly-occupied by an α-electron (the second α-electron navigates among the three excited orbitals). It occurs that our procedure is robust enough (and the ansatz expressible enough) that it did not end up at a local minimum. Indeed, it yields correct values of the three lowest targeted eigenenergies at convergence, but now sorted erratically along consecutive molecular geometries. While this went well here, a more systematic analysis should be made for assessing convergence properties under general circumstances.

3.1.1 Solving for eigenstates

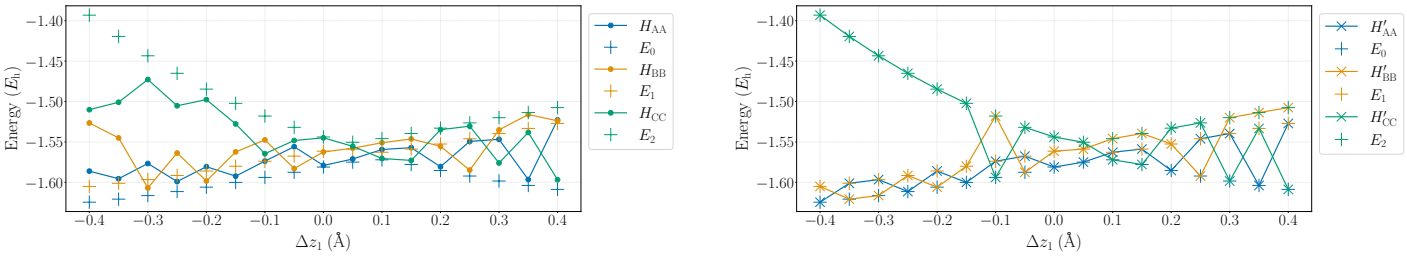

(a) After determining the subspace of minimal ensemble-energy

(b) After eigenstate resolution

Figure S2 Energies of the ensemble-VQE states: (a) $H_{\mathrm{AA}}, H_{\mathrm{BB}}, H_{\mathrm{CC}}$ after determining the subspace of minimal ensemble-energy; (b) $H'_{\mathrm{AA}}, H'_{\mathrm{BB}}, H'_{\mathrm{CC}}$ after eigenstate resolution (see Fig. 2, now using the initial state $|10000001\rangle$ and Eq. (20)). FCI energies of the first three eigenstates: E_0, E_1, E_2. Canonical MOs are used.

3.2 Distortion within C_1 geometry (from $\Delta x_2 = 0.1$ Å and $\Delta y_3 = 0.05$ Å): impact of the reference geometry

3.2.1 Achieving a quasi-diabatic representation: after determining the subspace of minimal ensemble-energy

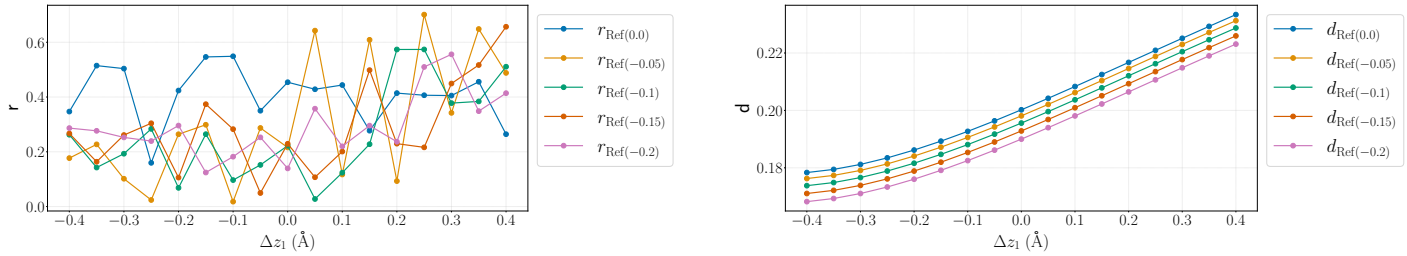

Figure S3 Diabaticity descriptors r and d using reference orbitals from various C_s geometries: $\Delta x_2^0 = 0.1$ Å for all, together with $\Delta z_1^0 = 0.0$ Å (Ref(0.0)), $\Delta z_1^0 = -0.05$ Å (Ref(0.05)), $\Delta z_1^0 = -0.1$ Å (Ref(-0.1)), $\Delta z_1^0 = -0.15$ Å (Ref(-0.15)), and $\Delta z_1^0 = -0.2$ Å (Ref(-0.2))

Fig. S3 shows that the descriptor r does not vary smoothly for any reference geometry $\boldsymbol{R}^0$ used to construct the diabatic MO basis. In contrast, the descriptor d varies smoothly and depends only slightly on the choice of $\boldsymbol{R}^0$. Moreover, similar behavior is observed for all reference geometries considered, and the differences between the corresponding curves remain nearly constant along the deformation coordinate. A more detailed analysis of these aspects will be provided in future work.

3.2.2 Achieving a quasi-diabatic representation: after descriptor r minimization

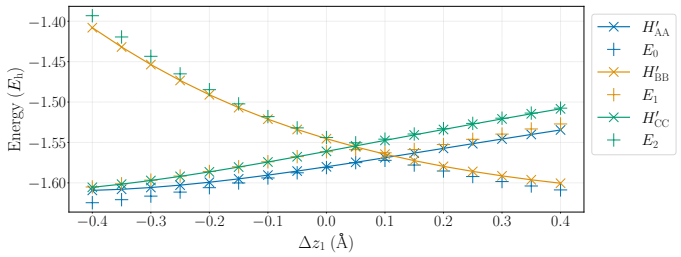

(a) Reference orbitals from Cs geometry: $\Delta x_2^0 = 0.1$ Å and $\Delta z_1^0 = 0.0$ Å

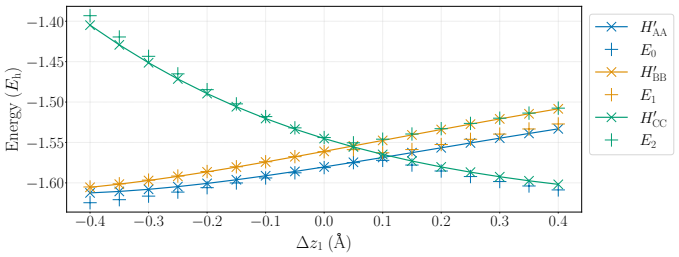

(b) Reference orbitals from Cs geometry: $\Delta x_2^0 = 0.1$ Å and $\Delta z_1^0 = -0.05$ Å

Figure S4 Energies of the ensemble-VQE states, $H'_{AA}, H'_{BB}, H'_{CC}$, and FCI energies of the first three eigenstates, E_0, E_1, E_2. Diabatic orbitals are used.

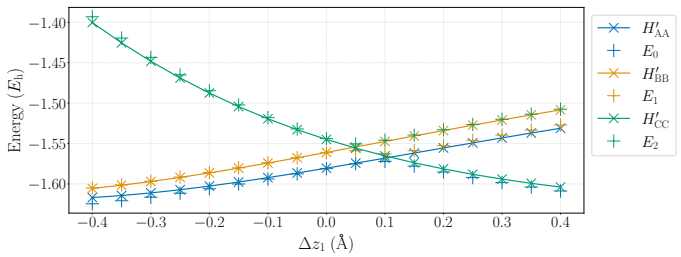

(a) Reference orbitals from Cs geometry: $\Delta x_2^0 = 0.1$ Å and $\Delta z_1^0 = -0.15$ Å

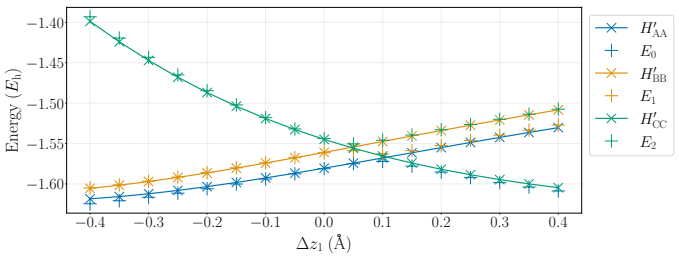

(b) Reference orbitals from Cs geometry: $\Delta x_2^0 = 0.1$ Å and $\Delta z_1^0 = -0.2$ Å

Figure S5 Energies of the ensemble-VQE states, $H'_{AA}, H'_{BB}, H'_{CC}$, and FCI energies of the first three eigenstates, E_0, E_1, E_2. Diabatic orbitals are used.

Fig. S4 and S5 show that small variations of the reference geometry $\boldsymbol{R}^0$ used to construct the diabatic MO basis induce slight variations in the optimized diabatic states, consistent with the behavior of the descriptor d observed in Fig. S3. The case where $\Delta x_2^0 = 0.1$ Å and $\Delta z_1^0 = -0.1$ Å is shown in the main text.

3.3 Distortion within C_s geometry (from $\Delta x_2 = 0.1$ Å and $\Delta y_3 = 0.0$ Å)

3.3.1 Solving for eigenstates

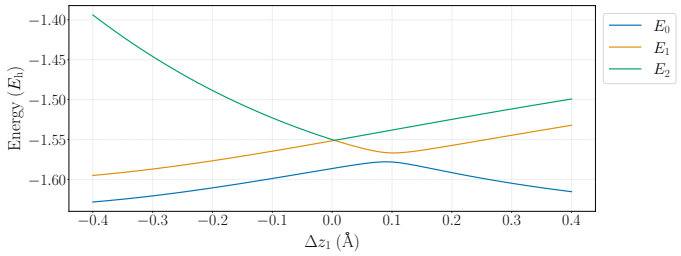

(a) (a)

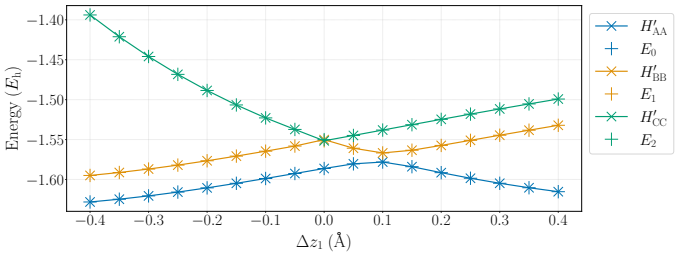

(b) (b)

Figure S6 (a) Adiabatic potential energies of the first three eigenstates, E_0, E_1, E_2, along Δz_1 obtained from a 'restricted open-shell Hartree–Fock' (ROHF) FCI/STO-3G calculation with Psi4[2]. (b) Energies of the ensemble-VQE states: $H'_{AA}, H'_{BB}, H'_{CC}$ after eigenstate resolution (see Fig. 2 and Eq. (20)). FCI energies of the first three eigenstates: E_0, E_1, E_2. Canonical MOs are used.

Fig. S6b shows that the ensemble retro-variational energies, $H'_{AA}, H'_{BB}, H'_{CC}$, fully match the eigenenergies as expected.

3.3.2 Achieving a quasi-diabatic representation: after determining the subspace of minimal ensemble-energy

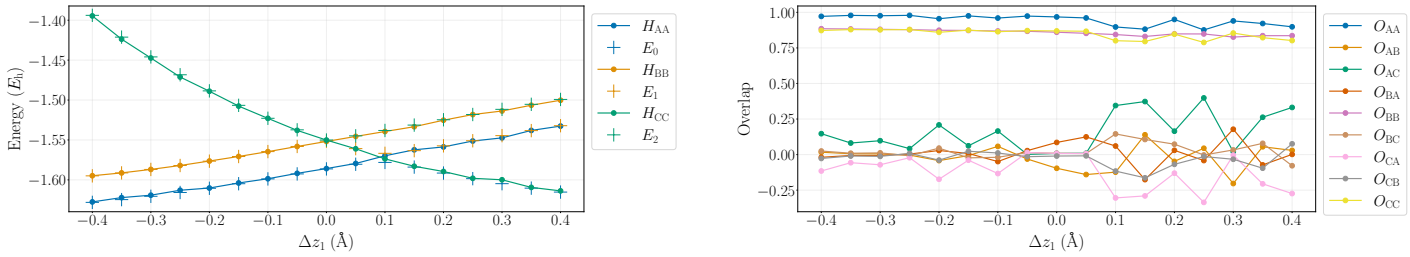

(a) **(b)**

Figure S7 (a) Energies of the ensemble-VQE states, H_{AA}, H_{BB}, H_{CC}, and FCI energies of the first three eigenstates, E_0, E_1, E_2. (b) CI-coefficient (overlap) submatrix elements of the ensemble-VQE states $\{|\Phi_I(\boldsymbol{t}^*)\rangle\}_{I\in\{A,B,C\}}$. Diabatic orbitals are used.

As in the case of the distortion within C_1 geometry, we chose, in the following, a C_s reference geometry, $\boldsymbol{R}^0$, for defining the diabatic orbitals[3], such that $\Delta x_2^0 = 0.1$ Å and $\Delta z_1^0 = -0.1$ Å. As seen in Fig. 4a, the energies of the states in Fig. S7a appear to follow a diabatic behavior, although they are not entirely smooth functions of the deformation coordinate. Fig. S7b indicates that the elements of the overlap matrix exhibit an irregular behavior similar to what is observed in Fig. 4b.

3.3.3 Achieving a quasi-diabatic representation: after descriptor r minimization

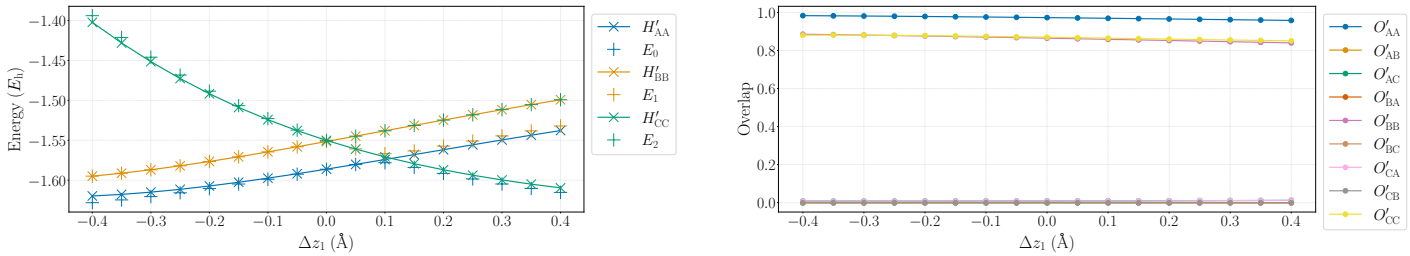

(a) **(b)**

Figure S8 (a) Energies of the ensemble-VQE states, $H'_{AA}, H'_{BB}, H'_{CC}$, and FCI energies of the first three eigenstates, E_0, E_1, E_2. (b) CI-coefficient (overlap) submatrix elements of the ensemble-VQE states $\{|\Phi'_I(\boldsymbol{t}^*, \theta_\star, \phi_\star, \psi_\star))\rangle\}_{I\in\{A,B,C\}}$. Diabatic orbitals are used.

From Fig. S8a, the diabatic energies obtained after minimization of the descriptor r appear smooth over the entire geometry profile. Moreover, the elements of the overlap matrix in Fig. S8b follow a behavior similar to that observed in Fig. 6b.

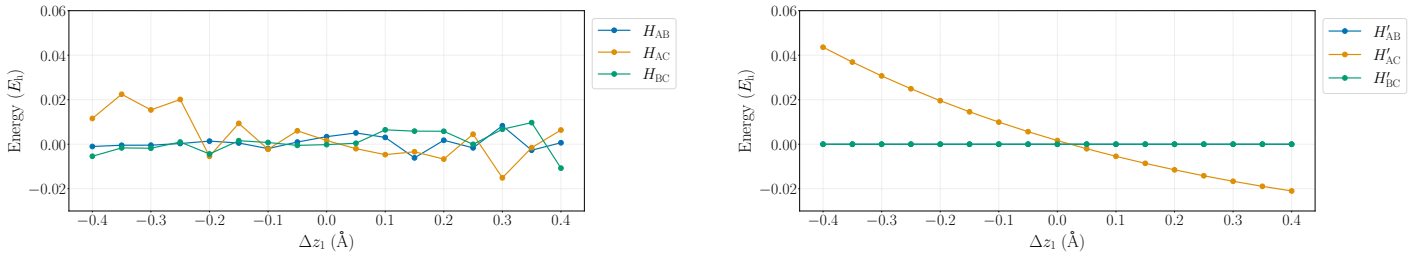

(a) **(b)**

Figure S9 (a) Off-diagonal Hamiltonian matrix elements in the basis of the ensemble-VQE states $\{|\Phi_I(\boldsymbol{t}^*)\rangle\}_{I\in\{A,B,C\}}$ (see Figs. S7a and S7b). (b) Off-diagonal Hamiltonian matrix elements in the basis of the ensemble-VQE states $\{|\Phi'_I(\boldsymbol{t}^*, \theta_\star, \phi_\star, \psi_\star)\rangle\}_{I\in\{A,B,C\}}$ (see Figs. S8a and S8b). Diabatic orbitals are used.

Fig. S9 indicates that the off-diagonal Hamiltonian matrix elements before the change of basis are not completely smooth, similarly to those shown in Fig. 7. After the change of basis, two out of the three off-diagonal Hamiltonian matrix elements become zero as expected from symmetry considerations.

3.4 Distortion from the T_d point group (from $\Delta x_2 = 0.0$ Å and $\Delta y_3 = 0.0$ Å) to the C_{3v} point group

3.4.1 Solving for eigenstates

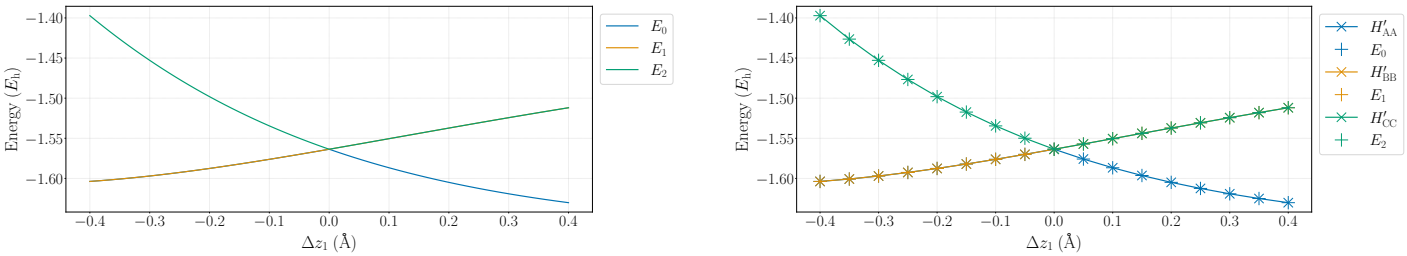

(a) (b)

Figure S10 (a) Adiabatic potential energies of the first three eigenstates, E_0, E_1, E_2, along Δz_1 obtained from a 'restricted open-shell Hartree–Fock' (ROHF) FCI/STO-3G calculation with Psi4[2]. (b) Energies of the ensemble-VQE states: $H'_{AA}, H'_{BB}, H'_{CC}$ after eigenstate resolution (see Fig. 2 and Eq. (20)). FCI energies of the first three eigenstates: E_0, E_1, E_2. Canonical MOs are used.

Fig. S10b shows that the ensemble retro-variational energies, $H'_{AA}, H'_{BB}, H'_{CC}$, fully match the eigenenergies as expected.

3.4.2 Achieving a quasi-diabatic representation: after determining the subspace of minimal ensemble-energy

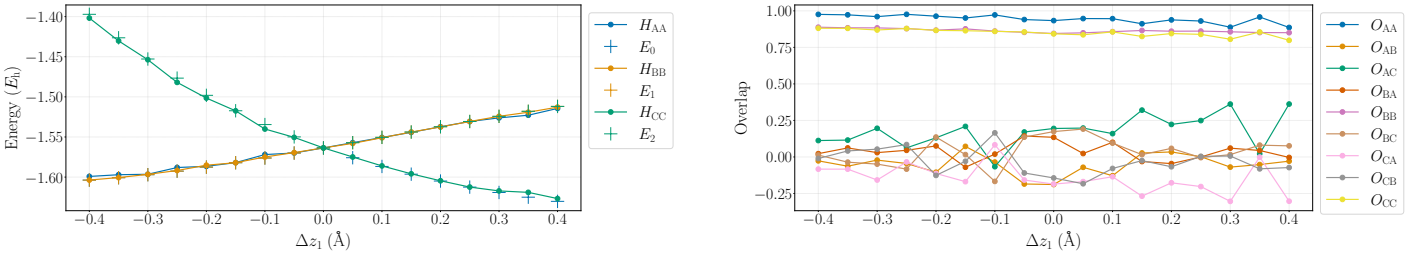

(a) (b)

Figure S11 (a) Energies of the ensemble-VQE states, H_{AA}, H_{BB}, H_{CC}, and FCI energies of the first three eigenstates, E_0, E_1, E_2. (b) CI-coefficient (overlap) submatrix elements of the ensemble-VQE states $\{|\Phi_I(\boldsymbol{t}^*)\rangle\}_{I\in\{A,B,C\}}$. Diabatic orbitals are used.

Similar observations as in Fig. 4 and Fig. S7 apply to Fig. S11, both regarding the state energies and the behavior of the overlap matrix elements. Moreover, it can be seen that for $\Delta z_1 = 0.0$ Å, corresponding to the T_d point, the energies of the three states are equal, as expected from symmetry considerations. In this case, the convergence of the ensemble energy imply that the energies of the ensemble-VQE states coincide with those of the eigenstates.

3.4.3 Achieving a quasi-diabatic representation: after descriptor r minimization

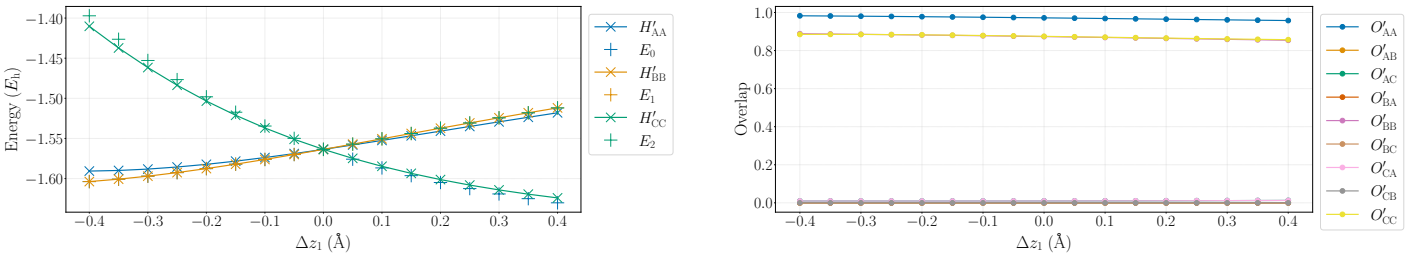

(a) (b)

Figure S12 (a) Energies of the ensemble-VQE states, $H'_{AA}, H'_{BB}, H'_{CC}$, and FCI energies of the first three eigenstates, E_0, E_1, E_2. (b) CI-coefficient (overlap) submatrix elements of the ensemble-VQE states $\{|\Phi'_I(\boldsymbol{t}^*, \theta_\star, \phi_\star, \psi_\star))\rangle\}_{I\in\{A,B,C\}}$. Diabatic orbitals are used.

Similar remarks to those made for Fig. 6 and Fig. S8 also apply to Fig. S12, both regarding the state energies and the overlap matrix elements.

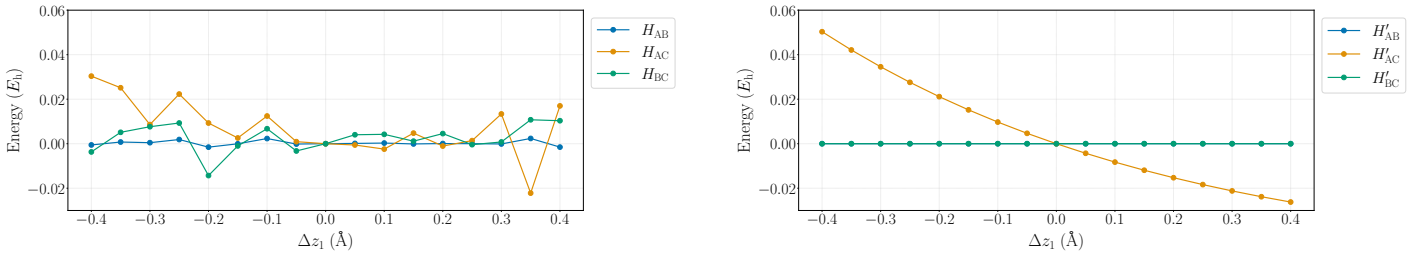

(a) **(b)**

Figure S13 (a) Off-diagonal Hamiltonian matrix elements in the basis of the ensemble-VQE states $\{|\Phi_I(\boldsymbol{t}^*)\rangle\}_{I\in\{\mathrm{A,B,C}\}}$ (see Figs. S11a and S11b). (b) Off-diagonal Hamiltonian matrix elements in the basis of the ensemble-VQE states $\{|\Phi'_I(\boldsymbol{t}^*,\theta_\star,\phi_\star,\psi_\star)\rangle\}_{I\in\{\mathrm{A,B,C}\}}$ (see Figs. S12a and S12b). Diabatic orbitals are used.

As observed Fig. 7 and Fig. S9, the off-diagonal Hamiltonian matrix elements before the change of basis are not entirely smooth in Fig. S13. The three off-diagonal Hamiltonian matrix elements vanish at $\Delta z_1 = 0.0$ Å which is consistent with the degeneracy of the energies of the three states observed Fig. S11a and expected from symmetry considerations. Moreover, after the change of basis, two out of the three Hamiltonian matrix elements become zero, in agreement with symmetry considerations.

Notes and references

[1] Emmanuel Laporte and Patrick Le Tallec. *Numerical Methods in Sensitivity Analysis and Shape Optimization*. Modeling and Simulation in Science, Engineering and Technology. Birkhäuser Boston, Boston, MA, 2003.

[2] Justin M. Turney, Andrew C. Simmonett, Robert M. Parrish, Edward G. Hohenstein, Francesco A. Evangelista, Justin T. Fermann, Benjamin J. Mintz, Lori A. Burns, Jeremiah J. Wilke, Micah L. Abrams, Nicholas J. Russ, Matthew L. Leininger, Curtis L. Janssen, Edward T. Seidl, Wesley D. Allen, Henry F. Schaefer, Rollin A. King, Edward F. Valeev, C. David Sherrill, and T. Daniel Crawford. Psi4: an open-source *ab initio* electronic structure program. *WIREs Computational Molecular Science*, 2(4):556–565, July 2012.

[3] Silvie Illésová, Martin Beseda, Saad Yalouz, Benjamin Lasorne, and Bruno Senjean. Transformation-Free Generation of a Quasi-Diabatic Representation from the State-Average Orbital-Optimized Variational Quantum Eigensolver. *Journal of Chemical Theory and Computation*, 21(11):5457–5480, June 2025.